Floquet and transient growth stability analysis of a flow through a compressor passage

G. Rocco [a,*], T.A. Zaki [b], X. Mao [d], H. Blackburn [c], S.J. Sherwin [a]

[a] *Department of Aeronautics, Imperial College London, South Kensington, London SW7 2AZ, UK*
[b] *Department of Mechanical Engineering, Imperial College London, South Kensington, London SW7 2AZ, UK*
[c] *Department of Mechanical and Aerospace Engineering, Monash University, Vic 3800, Australia*
[d] *School of Engineering and Computing Sciences, Durham University, Durham, UK*

A B S T R A C T

In this paper we investigate the instabilities arising in a flow through a compressor passage using BiGlobal stability analysis. The adopted geometry comes from the results of previous experimental and numerical investigations on a linear low-pressure (LP) compressor cascade [6,19,20]. Specifically, we address the role of laminar separation of the boundary layers at $Re = 138,500$, where such separation effects are enhanced by the strong adverse pressure gradients that the flow experiences, in contrast to the more commonly studied low-pressure (LP) turbines. The vortical structures downstream the separation bubble on the suction surface were recognised to show a well-defined time periodicity, which could be precisely detected. Floquet stability analysis was then used to investigate the response of the flow to infinitesimal perturbations. To overcome the difficulty of performing a Floquet stability analysis when the periodicity is restricted just to a small region of the domain, a phase-averaged base flow was computed, such that only the organised motions are extracted, neglecting all the background unsteadiness. The same technique allowed us to confirm the presence of strong energy transient growth phenomena, which are directly associated with convective instabilities occurring in the region downstream from the separation bubble.

© 2015 Published by Elsevier Masson SAS.

1. Introduction

Studies of flows in turbomachines are fundamental in aeronautical engineering and are currently subject to extensive investigations. These problems are particularly interesting due to the presence of relevant transitional phenomena. These phenomena are generally associated with high adverse pressure gradients with subsequent separation effects of the boundary layers and transition to turbulence. Wu and Durbin [17] performed simulations of flows in a T106 turbine cascade with periodically incoming wakes. They observed that the incoming wakes triggered turbulent spots along the suction surface, which prevented further separation effects; besides, two sets of streamwise vortices were observed on the pressure surface. Zaki and Durbin [18] demonstrate that the onset of turbulent spots can be explained by the interaction of free-stream turbulence with the lifted boundary-layer streaks. Jones et al. [9] simulated a flow over a NACA-0012 airfoil at 5° incidence at $Re = 5 \times 10^4$. The authors detected the presence of a laminar

separation bubble located at about 15% of the axial cord, where the breakdown to turbulence was observed; moreover, the flow was found to be absolutely unstable to three-dimensional perturbations. Abdessemed et al. [1] studied flow stability of a periodic array of a T106/300 low-pressure turbine blades at low Reynolds numbers ($Re < 5000$) using Floquet stability analysis and showed that for increasing Reynolds numbers the flow becomes unstable at progressively larger wavelengths. Although most studies focus on the low-pressure stages of turbines, several experimental and numerical investigations have been performed on flows in axial compressor geometries. Hughes and Walker [7] experimentally investigated separation effects of the boundary layer on the suction surface of a compressor blade at $1.1 \times 10^5 < Re < 1.3 \times 10^5$ and simulations of the role of the free-stream turbulence or incoming wakes have also been performed [19,20,12,13]. In particular, Zaki et al. [19,20] performed DNS of a NACA-0065 geometry, and detected a variety of transitional phenomena on both the pressure and suction surfaces. These phenomena were caused by both natural and by-pass mechanisms. The present study characterises the behaviour of a flow through a compressor passage at relatively high Reynolds number, $Re = 138,500$, from a stability perspective.

---

* Corresponding author.
  E-mail address: g.rocco10@imperial.ac.uk (G. Rocco).

In the configuration adopted in this paper, due to the high adverse pressure gradient along the suction surface of the blade, the boundary layer profiles become inflectional and the flow might show an instability and high sensitivity to initial disturbances. Moreover, perturbations downstream of the separation bubble are subject to curvature of the blade and unsteadiness of the flow [20]. Therefore, local studies at a fixed streamwise location are not able to describe properly the dynamics of the system, which is characterised by distinct vortex shedding along the suction surface. Global stability studies by means of a time-averaged mean flows were shown to predict the frequency of the vortex shedding [2]. However, since a well-defined periodicity of the flow is detected on the suction surface, downstream from the separation bubble, Floquet analysis is ideal to characterise transition. Unfortunately, this is not a feasible approach because this periodicity is just in a restricted part of the domain. To overcome this limitation, we adopt a phase-averaged base flow [5]. This approach allowed us to evaluate the behaviour of transition by computing the leading Floquet mode at different spanwise lengths and the presence of convective instabilities.

2. Numerical methods and discretisation

The governing equation for an incompressible viscous flow are:

$$\frac{\partial \mathbf{u}}{\partial t} + \mathbf{u} \cdot \nabla \mathbf{u} = -\nabla p + \frac{1}{Re} \nabla^2 \mathbf{u} \tag{1a}$$

$$\nabla \cdot \mathbf{u} = 0 \tag{1b}$$

where $\mathbf{u}$ is the velocity field, t is the time, p the static pressure and $Re = U_\infty L / \nu$ is the Reynolds number, defined by means of the characteristic length of the domain L, the free-stream flow velocity U_∞ and μ is the kinematic viscosity. To study the stability of a flow, we decompose the flow field into the sum of a two-dimensional base state $\mathbf{U}$ and three-dimensional perturbations $\mathbf{u}'$, $\mathbf{u} = \mathbf{U} + \mathbf{u}'$. Substituting into (1) and neglecting the second order terms $O(\mathbf{u}'^2)$, we obtain the linearised Navier–Stokes equations.

$$\frac{\partial \mathbf{u}'}{\partial t} + \mathbf{U} \cdot \nabla \mathbf{u}' + \mathbf{u}' \cdot \nabla \mathbf{U} = -\nabla p' + \frac{1}{Re} \nabla^2 \mathbf{u}' \tag{2a}$$

$$\nabla \cdot \mathbf{u}' = 0 \tag{2b}$$

Taking the divergence of (2a) and enforcing (2b), we can write the problem as (3), where $\mathcal{A}$ is a linear operator which encapsulates the time evolution of the perturbations:

$$\frac{\partial \mathbf{u}'}{\partial t} = \mathcal{A}(\mathbf{U})\mathbf{u}' \tag{3}$$

We assume the perturbations to be the product of a spatial and temporal term $\mathbf{u}'(\mathbf{x}, t) = \hat{\mathbf{u}}(x, y) \exp(i\beta z + \lambda t)$, where $\beta = 2\pi / L_z$ and $\lambda \in \mathbb{C}$; the problem is then shifted to the solution of the eigenproblem of the associated operator $\mathcal{A}$. In the present work the base flows will be computed solving the non-linear Navier–Stokes equations (1) and these solutions will then be used to evaluate the dominant eigenvalues and eigenvectors of the linearised operator $\mathcal{A}$. The solution of the eigenproblem is obtained by an Arnoldi algorithm based on the earlier work of Barkley et al. [3] and Tuckerman and Barkley [15].

3. Geometry and discretisation

The blade geometry is a NACA-65 airfoil at Reynolds number $Re = 138{,}500$, which is identical to previous studies performed by Zaki et al. [19,20]. Although this value is below the normal operating conditions of aeronautical engines, this analysis is aimed
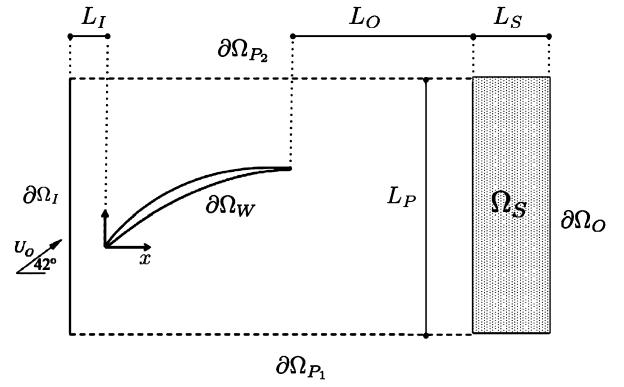

Fig. 1. Sketch of the geometry of the problem.

at understanding the relevant instability mechanisms involved for this geometry. At this Reynolds number transition was seen to be rather slow, therefore, in all the simulations performed in this paper the flow can be considered laminar. The linear low pressure (LP) compressor cascade is based on the experimental studies performed at the University of Armed Forces in Munich (further details and discussions about the geometry can be found in [6]). Similar to Zaki et al. [19,20], we will consider just one passage of the compressor, using periodic boundary conditions on the upstream and downstream boundaries of the domain. The use of periodic boundary conditions to simulate such flows has already been used in the context of turbine passages [17,16] and it generates synchronous vortex shedding of the trailing-edge vortices. The BiGlobal stability analysis performed by Abdessemed et al. [1] on low-pressure turbine (LPT) blades showed that the adoption of two passages affects the dynamics of the shedding, which become asynchronous with relevant effects on the stability. However, as Zaki et al. [20] noted, this phenomenon is relevant for the geometries where the flow is subject to strong turning effects. In the present configuration the velocity at the trailing edge of the blade is nearly horizontal and does not interact with the upstream flow, therefore no asynchronicity is present. Fig. 1 shows a sketch of the geometry used. The vertical length of the domain L_p corresponds to one blade pitch $L_p \simeq 0.6L$, where L is the axial chord of the blade. The inflow boundary $\partial \Omega_I$ is at a distance $L_I = -0.4L$ from the leading edge, while the outflow $\partial \Omega_O$ is at a distance $4L$ from the trailing edge. As already mentioned, periodic boundary conditions were used on the lower and upper boundaries ($\partial \Omega_{P_1}$ and $\partial \Omega_{P_1}$ respectively), while a velocity $(U_0 \cos(\alpha), U_0 \sin(\alpha))$ was assigned at the inflow boundary $\partial \Omega_I$, where $\alpha = 42°$ and $U_0 = 1$. This configuration corresponds to the angle of attack at design, since its actual value in experiments could not be measured reliably. As discussed by Zaki et al. [20], this choice generates some differences in the pressure distribution, but does not affect the mechanisms related to the boundary layer separation and transition. To avoid numerical instabilities, an absorbing layer was used in the outflow region $\partial \Omega_O$ [8], which allows disturbances to pass out of the region of interest into a limited small region where they are dissipated. This can be achieved by adding a damping momentum forcing to the Navier–Stokes equations, $\mathbf{F} = -D(\mathbf{u} - \mathbf{u}|_{\partial \Omega_O})$, where D is the damping coefficient and is different from zero only in the damping region, while $\mathbf{u}|_{\partial \Omega_O}$ is the velocity on the boundary. Homogeneous Neumann boundary conditions were used for the velocity on the downstream boundary $\partial \Omega_O$. The streamwise length of the artificial dumping region is $L_S = L$, while the damping coefficient was set to $D = 50$, which was sufficiently large to avoid numerical instabilities. No-slip boundary conditions were applied on the surface of the blade. In summary, the following boundary conditions were adopted:
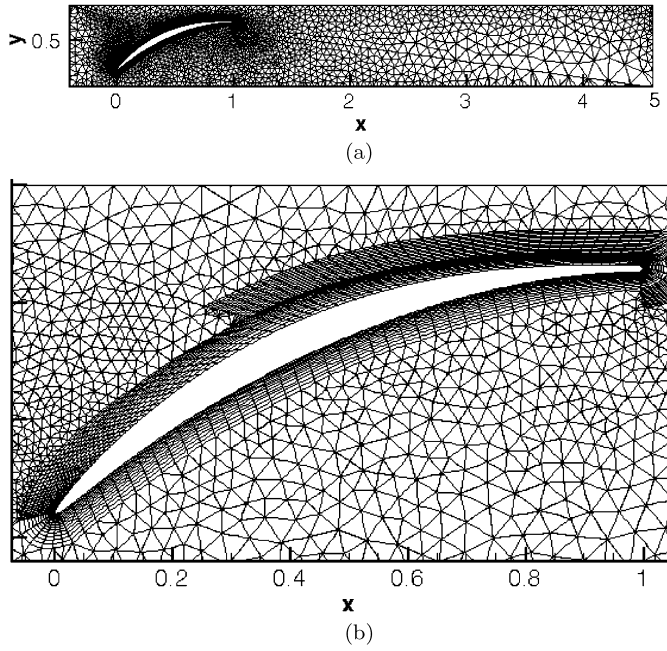
Fig. 2. (a) Mesh adopted for the simulations. (b) Detail of the submesh around the surface of the blade.

$$\partial\Omega_W := \begin{cases} u = 0, \\ v = 0 \end{cases} \tag{4a}$$

$$\partial\Omega_I := \begin{cases} u = \cos(42°) \simeq= 0.7431 \\ v = \sin(42°) \simeq= 0.6691 \end{cases} \tag{4b}$$

$$\partial\Omega_O := \begin{cases} \frac{\partial u}{\partial x} = 0 \\ \frac{\partial v}{\partial x} = 0 \end{cases} \tag{4c}$$

$$\partial\Omega_{P_{1,2}} := \begin{cases} u|_{\partial\Omega_{P_1}} = u|_{\partial\Omega_{P_2}} \\ v|_{\partial\Omega_{P_1}} = v|_{\partial\Omega_{P_2}} \end{cases} \tag{4d}$$

We note that the grid topology blade is slightly different from the case presented by Zaki et al. [19] and Wu and Durbin [17], where the pressure and suction surfaces were incorporated into the boundaries of the computational domain. Our choice facilitates local refinement of the leading and trailing edges, to guarantee reliable results of stability analysis. This geometry was discretised using a spectral/hp element method with roughly 6000 elements, as shown in Fig. 2a. The mesh is hybrid and composed of both triangular and quadrilateral elements. Close to the surfaces of the blade, where relevant separation effects are observed, a structured sub-mesh of quadrilaterals is adopted (Fig. 2b), while triangles are used in the remaining part of the domain. Modal bases were used for interpolation using 8th order polynomials [11]. Finally, a stiffly stable time splitting scheme [10] was adopted to solve the Navier–Stokes equations, using a second-order time integration technique with a time step $\Delta t = 1 \times 10^{-5}$. High-order pressure boundary conditions [10] were applied on the inflow and wall boundaries, whereas a Dirichlet condition was applied on the outflow boundary $\partial\Omega_O$.

4. Description of the base flow

In this section we describe the base flow which provides an insight into the physical mechanisms occurring on both the pressure and suction surfaces. Furthermore, it provides a validation of our discretisation with respect to the previous results [20]. An important consideration is the distribution of time-averaged pressure coefficient, defined as $C_P := (P - P_{ref})/(\rho U_0^2/2)$, where ρ is the density of the flow and P_{ref} a reference total pressure, which is
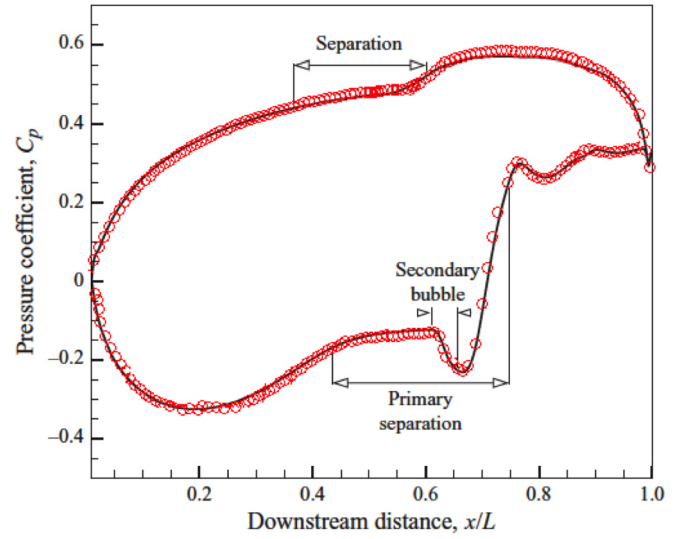

Fig. 3. Distribution of the pressure coefficient C_p along the surface of the blade. Solid line represents the result from [20], while hollow circles the present results.

the inflow pressure in the present case. Fig. 3 shows the profile of the pressure coefficient over the surface of the blade. The data are compared with the results obtained by Zaki et al. [20] and provide a validation of the discretisation at the parameters summarised in the previous section. The top curve represents the pressure surface, where an adverse pressure gradient is established up to about $x/L \simeq 0.8$, followed by a region of favourable pressure gradient. At $x/L \simeq 0.55$ the curve shows a mild separation of the boundary layer. As described by Zaki et al. [20], a more pronounced separation occurs on the suction surface where the flow is subject to a strong acceleration until $x_L \simeq 0.2$, followed by a strong adverse pressure gradient. This is responsible for an evident flow separation, and in absence of free-stream perturbations (turbulence wakes or free-stream turbulence), a Kelvin–Helmholtz instability arises. However, the vortical structures do not break up to turbulence and remain in proximity of the surface of the blade. A small region of reverse flow can be detected on the suction surface even after the rolls are convected downstream; this region is known as *secondary bubble* and it moves at the same velocity of the Kelvin–Helmholtz rolls. A more detailed discussion of the behaviour of the pressure coefficients and the physical phenomena can be found in [20] and [6].

All these physical mechanisms are apparent in the contours of the instantaneous spanwise vorticity ω_z around the surface of the blade (Fig. 4). To characterise the behaviour of these structures, we consider the profiles of the velocity along the separation region of the suction side. Specifically, we track the time evolution of the velocity at 4 points, $P_1 \equiv (x_1, y_1) = (0.66, 0.65)$, $P_2 \equiv (x_2, y_2) = (0.73, 0.67)$, $P_3 \equiv (x_3, y_3) = (0.82, 0.67)$, $P_4 \equiv (x_4, y_4) = (0.93, 0.68)$, which are distributed along the separation region of the suction surface where the vortical structures were detected. The time evolution of the velocity shows a clear periodic behaviour of the structures, confirmed by the presence of a limit cycle (Figs. 6–8). A total period $T = 0.22$ can be clearly identified, which corresponds to a complete shedding cycle, as shown in Fig. 5. In the other parts of the domain, no other straightforward periodicity could be detected.

5. Phase-averaged base flow and Floquet stability analysis

To characterise the stability of the Kelvin–Helmholtz rolls, we need to perform linear stability analysis. Floquet stability analysis requires time-periodicity and is therefore not applicable on the
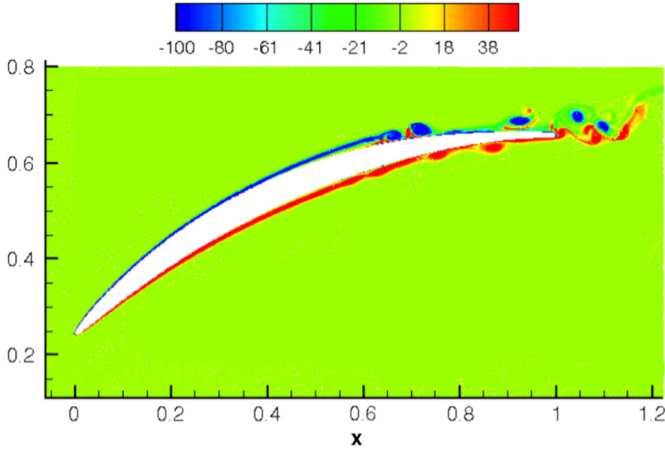
Fig. 4. Profile of the spanwise vorticity ω_z.

whole domain. An alternative approach is the computation of a phase-averaged mean flow. This technique allows us to sort the flow into several groups, each corresponding to a small interval associated with the phase of the shedding cycle. Following Cantwell and Coles [5], we divided the N samples into a specific number of subpopulations N_P, 50 in the present study, each one associated with a particular phase interval of the shedding. Within each subpopulation, composed by N_i samples, we can define a mean at constant phase $\langle \boldsymbol{u} \rangle$:

$$\langle \boldsymbol{u} \rangle = \frac{1}{N_i} \sum_{j=1}^{N_i} \boldsymbol{u}_j \quad i = 1, 2, \ldots, N_P \tag{5}$$

The adoption of a phase-averaging technique to approximate the base-flow can be shown to be more precise than Reynolds-averaged base-flows, in fact it leads to a minimisation of the contributions of the Reynolds stresses, by which the RANS and the Navier–Stokes solution differ [5]. This leads to smaller approximation errors and is important especially in the context of linear stability analysis. Figs. 9 and 10 show the profiles of the
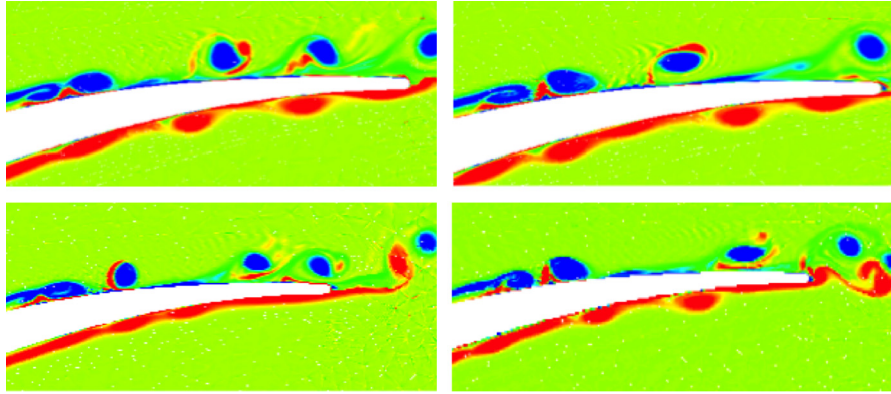

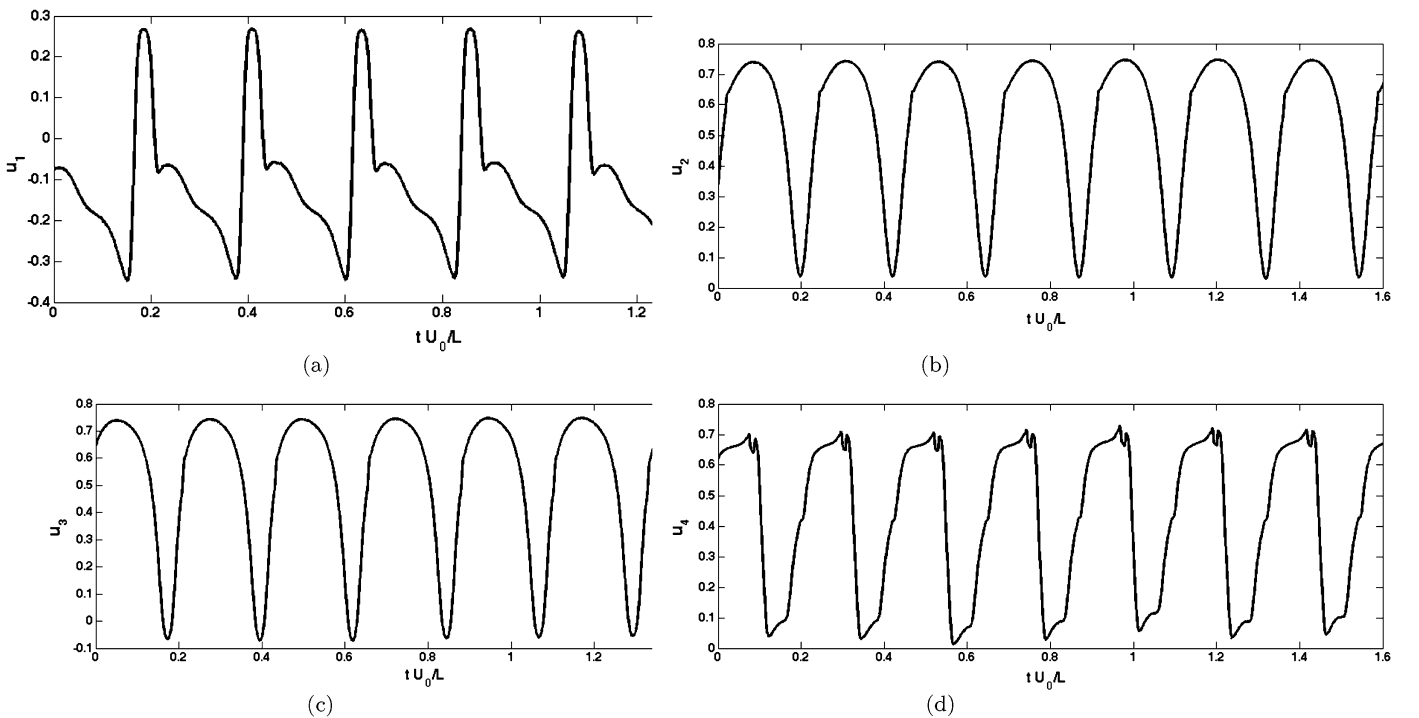**Fig. 5.** Vorticity profile for four different phases of the shedding cycle.

Fig. 6. Time evolution of the streamwise velocity u'; (a) $P_1 \equiv (x_1, y_1) = (0.66, 0.65)$, (b) $P_2 \equiv (x_2, y_2) = (0.73, 0.67)$, (c) $P_3 \equiv (x_3, y_3) = (0.82, 0.67)$, (d) $P_4 \equiv (x_4, y_4) = (0.93, 0.68)$.
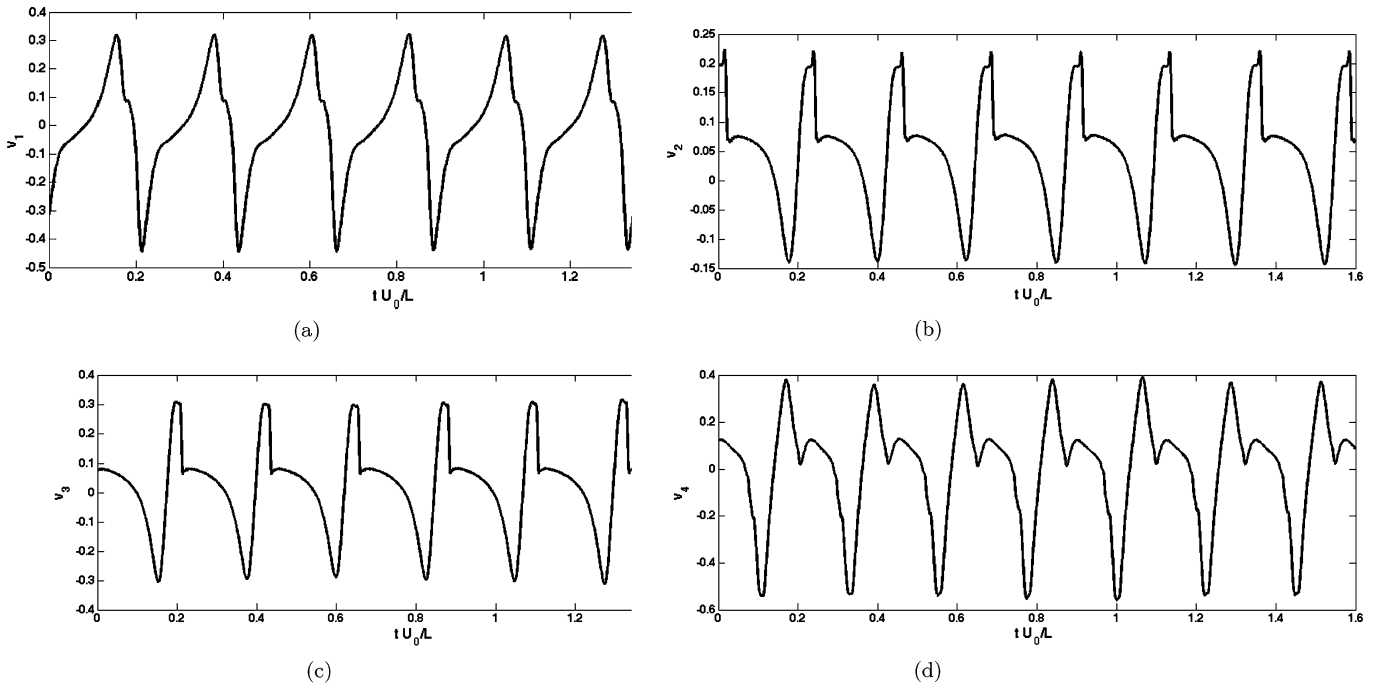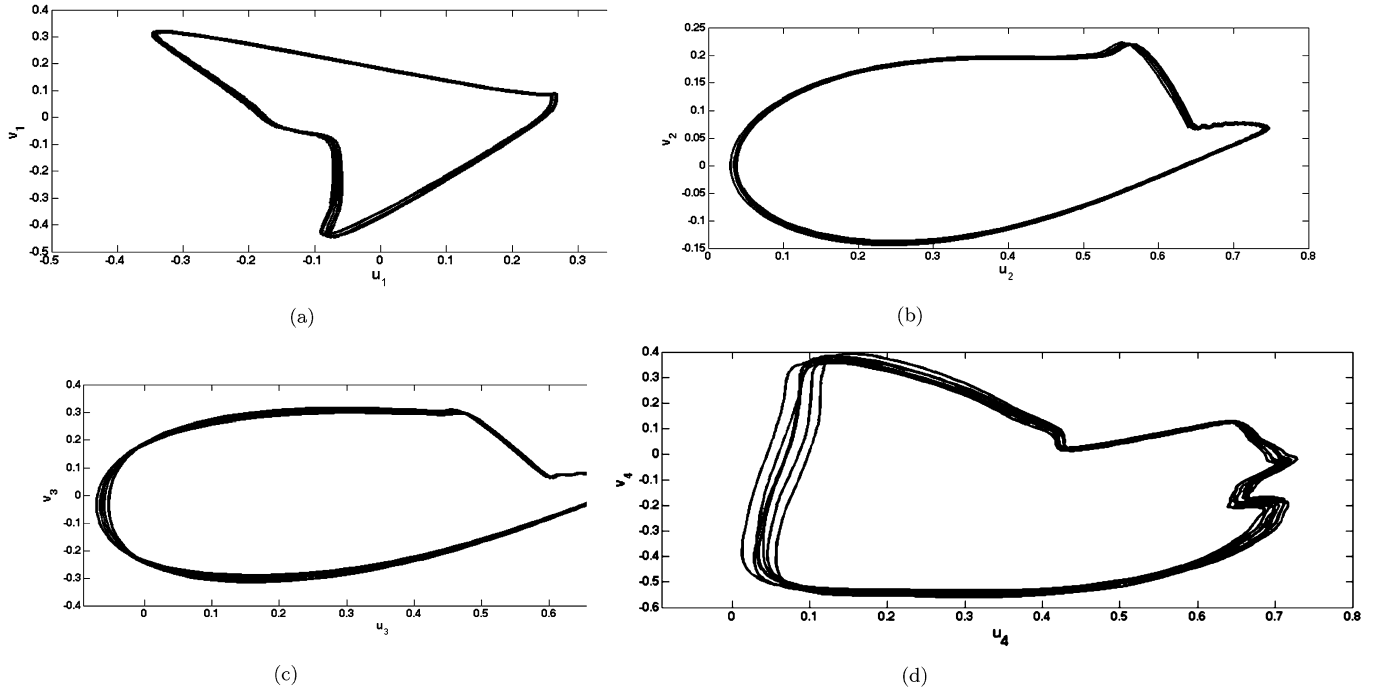
Fig. 7. Time evolution of the transverse velocity v'; (a) $P_1 \equiv (x_1, y_1) = (0.66, 0.65)$, (b) $P_2 \equiv (x_2, y_2) = (0.73, 0.67)$, (c) $P_3 \equiv (x_3, y_3) = (0.82, 0.67)$, (d) $P_4 \equiv (x_4, y_4) = (0.93, 0.68)$.

Fig. 8. Detection of the limit cycle of the transverse component v as a function of the streamwise component u; (a) $P_1 \equiv (x_1, y_1) = (0.66, 0.65)$, (b) $P_2 \equiv (x_2, y_2) = (0.73, 0.67)$, (c) $P_3 \equiv (x_3, y_3) = (0.82, 0.67)$, (d) $P_4 \equiv (x_4, y_4) = (0.93, 0.68)$.

phase-averaged vorticity at four different phases, where the phase-averaging was performed over 100 cycles. Almost all the unsteady phenomena on the pressure surface have been smeared out by the averaging, while the roll-up of the boundary layer due to a Kelvin–Helmholtz instability is still detectable on the suction surface.

5.1. Floquet stability analysis

The phase-averaged base flow was examined in terms of its capacity to amplify three-dimensional disturbances, using the

BiGlobal approach [14]. Floquet analyses at different spanwise wavenumbers $\beta = 2\pi/L_z$ were performed to study the stability of the periodic states which characterise the region downstream from the separation bubble. The solution of the eigenproblem was performed using a Krylov subspace $m = 12$ and the tolerance on the eigenvalues was set to 10^{-5}. Tests with $m \geq 12$ produced differences in the magnitudes of the leading Floquet modes of order 10^{-4}. Fig. 11 shows the eigenspectrum, which reports the value of the Floquet multipliers with respect to eight different eight values of the wavenumber β. All the Floquet mul-
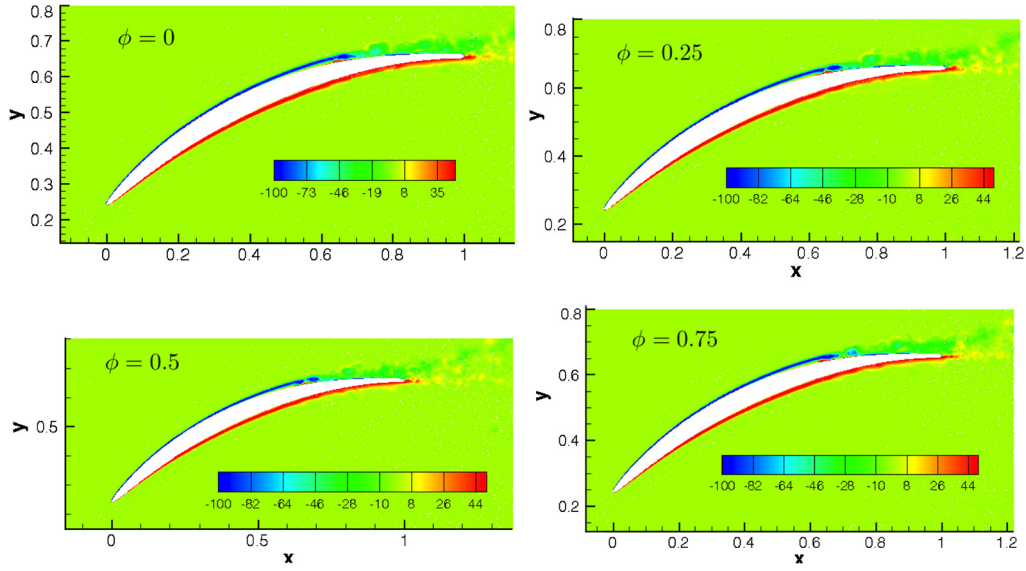
Fig. 9. Contours of the phase-averaged vorticity at four different phases.
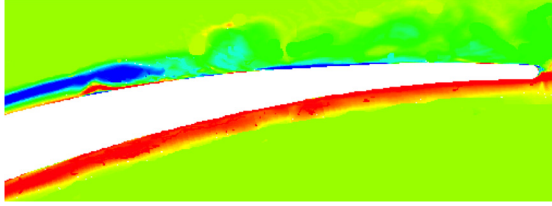

Fig. 10. Detail of the phase-averaged base flow at $\phi = 0$, near the trailing edge.

tipliers are real and $|\mu| < 1$ denotes a decaying perturbation, while $|\mu| > 1$ a growing one. Therefore, they are related to stable and unstable modes respectively. An unstable Floquet mode was detected just for very small wavenumbers, $\beta < \pi/10$, where the magnitude of the leading Floquet multiplier, $|\mu|$, is greater than the unit value. This result is similar the findings of [1], who suggested that in a low-pressure turbine, the instabilities arise at $\beta \to 0$ when $Re \to \infty$. Since the instability is region is present in a very small range of wavenumbers and is expected to become less prominent when the Reynolds number is increased.

Since the region where the instability arises is in a very small range of wavenumbers, and is expected to disappear for higher Re, it is not investigated in this paper. However, the structure of the Floquet mode does not appear to be dissimilar from the one found in the stable region. The structure of the normalised Floquet mode at $\beta = 500$ is reported in Fig. 12; the mode is located on the suction side, across the separation bubble, where the unsteady phenomena of the phase-averaged base flow were observed. Its intensity becomes weaker approaching to the trailing-edge and, despite that the general structure of the mode appears to be rather complex, a wake pattern can still be detected. The contributions of the velocity components $\hat{u}'$, $\hat{v}'$, $\hat{w}'$ is shown in Fig. 13.

We can validate the results of the Floquet analysis superposing the Floquet mode to the base flow $\boldsymbol{u}(x, y, t) + \varepsilon \hat{\boldsymbol{u}}'(x, t) \exp(\omega t + \beta z)$ and use the result as initial conditions to integrate the non-linear Navier–Stokes equations. In the present case, we chose $\varepsilon = 10^{-6}$ and the energy of the system $E = \frac{1}{2} \int_\Omega \|\boldsymbol{u}\|^2 d\Omega$ as a function of the non-dimensional time is reported in Fig. 14. The growth rate obtained from the DNS, corresponding to the slope of the curve at $t \simeq 0$, was found to be 0.885, while the stability analysis pre-
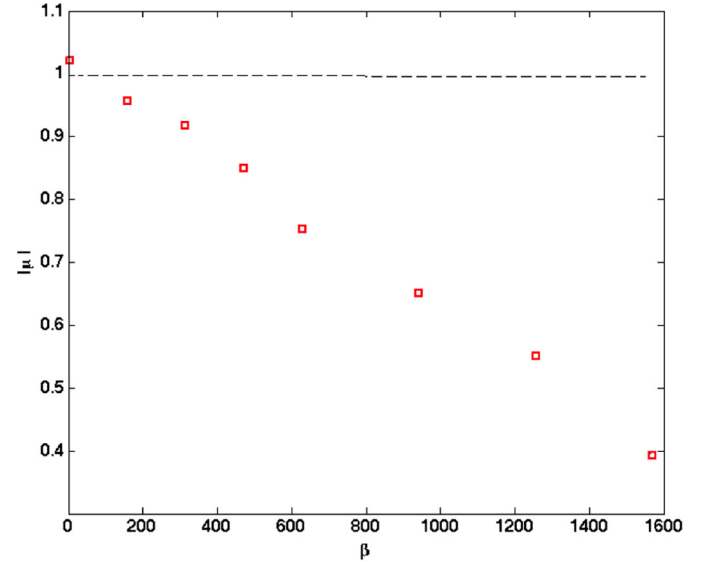

Fig. 11. Floquet multipliers $|\mu|$ as a function of the wavenumbers β. Unstable mode corresponds to $\beta = \pi/10$.
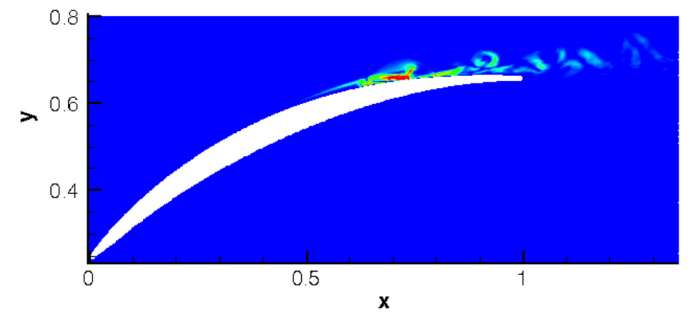

Fig. 12. Magnitude of the dominant Floquet mode at $\beta = 500$.

dicted a value $\mu = 0.891$. The difference of these two values is of order 10^{-3} and can be attributed mainly to the adoption of the phase-averaged base flow, which includes the additional presence of the Reynolds stresses, and the non-linearities of the Navier–Stokes equations.
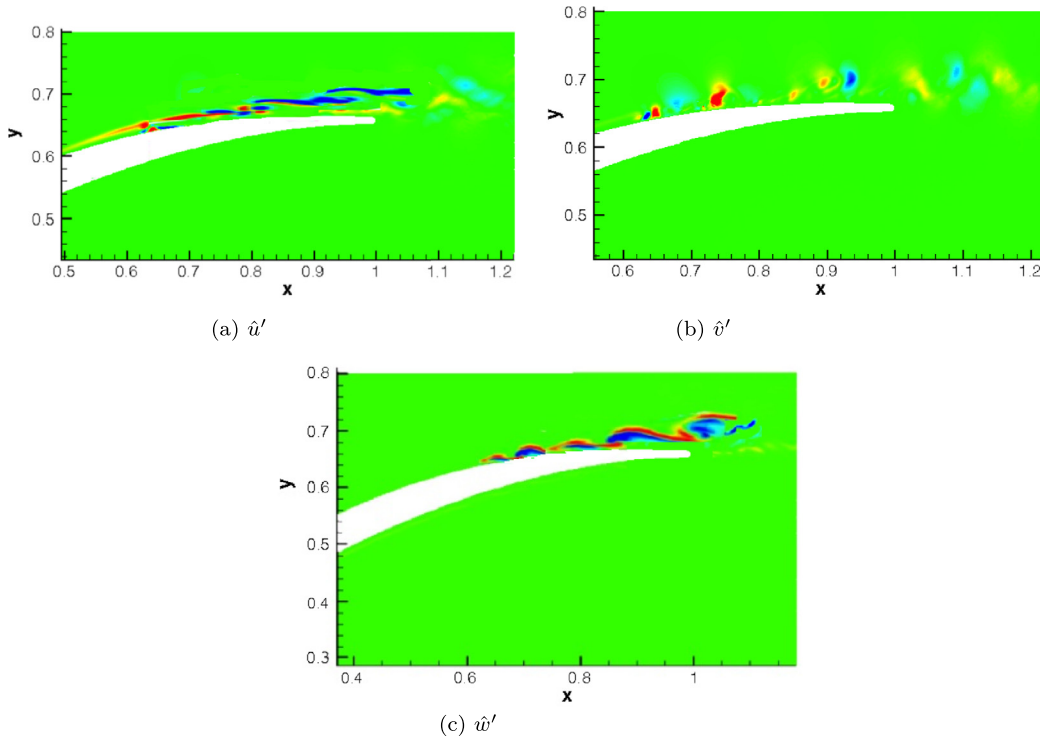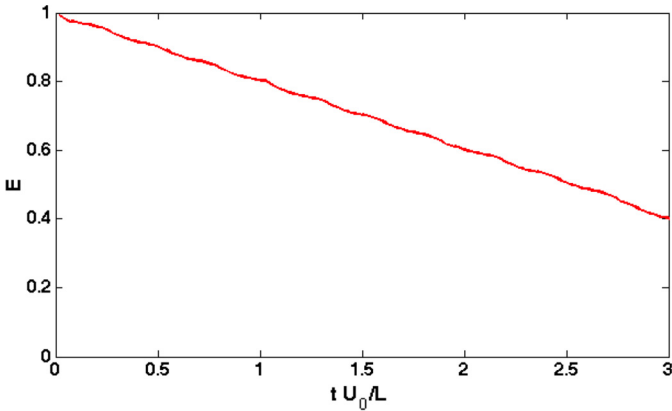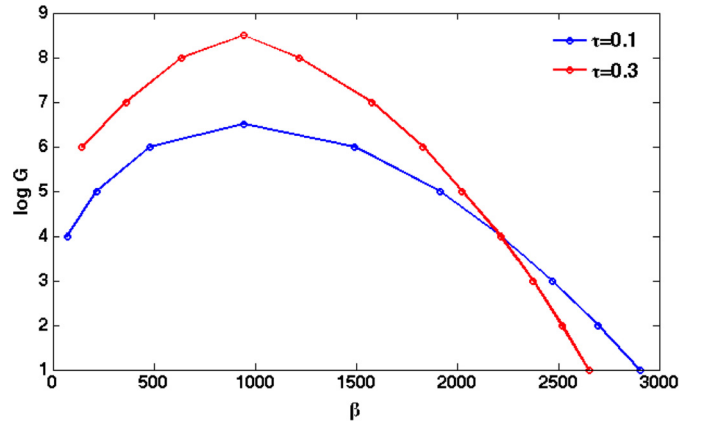
(a) $\hat{u}'$

(b) $\hat{v}'$

(c) $\hat{w}'$

Fig. 13. Velocity components of the Floquet mode.

Fig. 14. Time evolution of the energy of eigenmode associated with $\beta = 500$. The curve was obtained by a non-linear Navier–Stokes simulation.

Fig. 15. Variation of the optimal energy growth G with the spanwise wavenumber β for two different time horizons: $\tau = 0.1$ and $\tau = 0.3$ respectively.

6. Transient growth analysis

The Floquet analysis performed in the previous section pointed out that the flow is asymptotically stable at almost every wavenumber. However, the interaction of stable modes might generate large energy transient growth phenomena. This observation is consistent with the presence of a region, downstream from the separation bubble, characterised by a significant concentration of energy. Transient growth analysis was then performed by means of the adjoint loop optimisations described in [3]; the base flow consists again of 50 time slices, obtained by phase-averaging the non-linear Navier–Stokes equations, corresponding to one shedding cycle $T = 0.22$. The computational parameters are unaltered with respect to Floquet analysis, except for the Krylov subspace dimension which was chosen to be $m = 5$. Two different time horizons were investigated, $\tau = 0.1$ and $\tau = 0.3$ respectively. The variation of the energy growth with the spanwise wavenumber β is shown in Fig. 15. Both cases are convectively unstable in a wide range of spanwise wavenumbers, hence significant energy transient

growth phenomena are present. The most energised wavenumber is $\beta \simeq 400\pi$ in both cases, which corresponds to a wavelength $L_z = 1/200$.

Transient growth analysis confirms the prominent role of the convective instabilities, showing significant energy amplification. These values are comparable with results obtained for flows over a backward facing step [4]. The profiles of the vorticity of the optimal perturbations are reported in Fig. 16; in both cases the optimal perturbations are located near the separation bubble and are convected downstream from the suction surface, exploiting the shear region of the base flow. However, two different topologies can be detected for these optimal perturbations: the optimal perturbation at $\tau = 0.1$ has the shape of a thin shear layers, while the one at $\tau = 0.3$ extends over 10% of the axial chord from the primary separation region and it is composed of an array of alternating vortical structures. The profile of the optimal perturbations and the high growth rate of the instabilities show that the region downstream from the separation bubble, where the periodic phenomena where
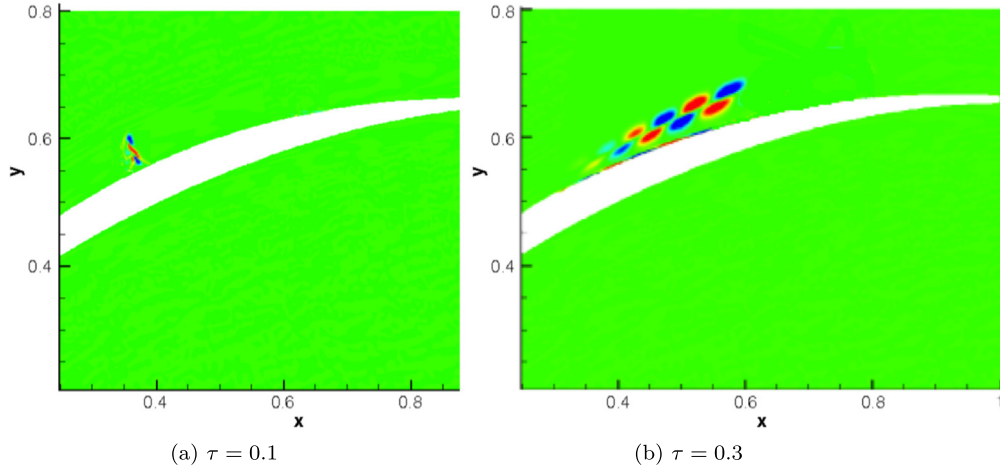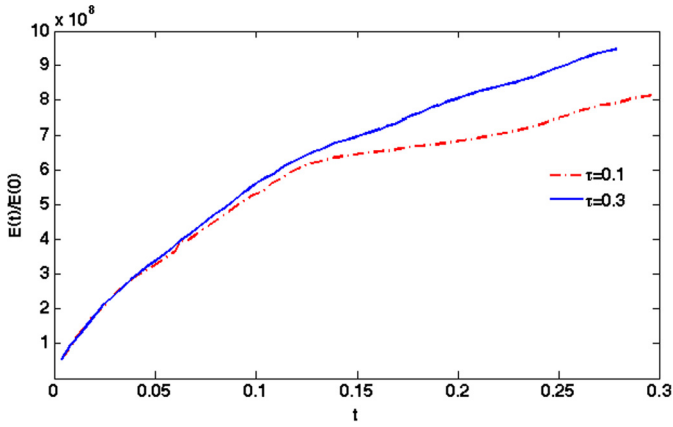
(a) $\tau = 0.1$ (b) $\tau = 0.3$

Fig. 16. Spanwise vorticity of the optimal perturbations.

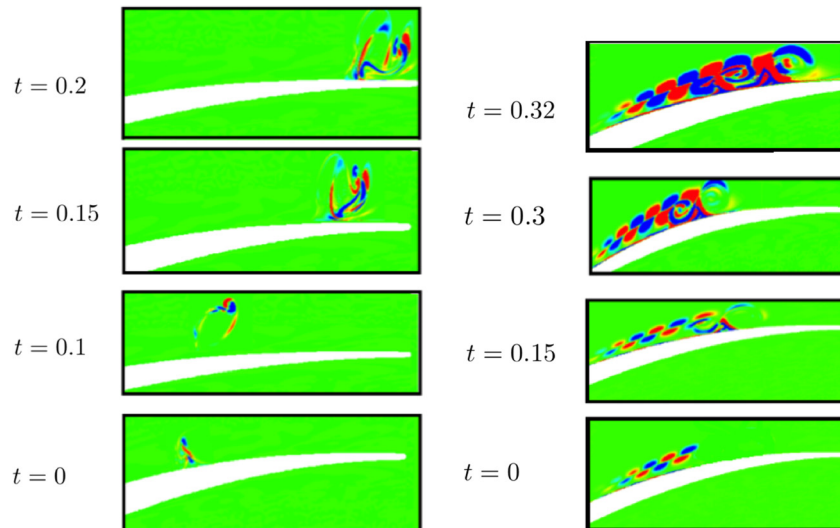**Fig. 17.** Transient responses at $\beta = 400\pi$ for two times horizons ($\tau = 0.1$ and 0.3).

observed, is crucial for triggering convective instabilities and nonlinear mechanisms to transition.

The energy evolution of these second optimal disturbances is reported in Fig. 17 for the two time horizons. This profile is obtained by time-marching the linearised Navier–Stokes equations using the optimal perturbations as initial conditions. For $t \leq 0.05$ the two curves are practically overlapped, but for longer times the

energy growth associated with $\tau = 0.3$ is subject to a larger amplification. These behaviours are characteristic of the small time horizons we considered; if τ is large enough, the perturbations are expected to be convected further downstream and the energy amplification would drop. Fig. 18 shows the time evolution of the disturbances. For $\tau = 0.15$ the thin shear layer rolls up while being convected along the suction surface, experiencing a progressive increase in its strength. The optimal perturbation corresponding to $\tau = 0.3$ is instead subject to an Orr mechanisms which results into a Kelvin–Helmholtz instability, confirming the results obtained by the DNS.

7. Conclusions

In this paper we performed stability analysis of a flow over a NACA-65 airfoil at $Re = 138,500$. Direct numerical simulations were performed to validate the discretisation and the computational parameters with the previous findings reported by Zaki et al. [20]. Besides, DNS allowed us to understand the prominent role of the pressure gradients on the pressure and suction surface. Specifically, the adverse pressure gradient on the suction surface generates an inflection of the boundary layers, which is subject to a Kelvin–Helmholtz instability. The vortical structures were verified to remain coherent with a well-defined periodicity which was clearly identified. A phase-averaging technique was adopted to ex-

Fig. 18. Time evolution of the optimal perturbations. (a) $\tau = 0.1$, (b) $\tau = 0.3$.

tract only the organised vortical structures and it consists of an average of a large ensemble of states with the same phase with respect to a reference oscillator. Such approach allowed us to sort the flow in 50 time slices and the Floquet stability analysis was performed for different spanwise wavenumbers β. The leading Floquet multipliers were found to be real and the flow was seen to be unstable just for very small wavenumber ($\beta < \pi/10$). The leading eigenmode showed a concentration of energy in the region of the separation bubble, suggesting the presence of relevant energy transient growth phenomena. Therefore a transient growth analysis was performed for two time horizons, $\tau = 0.1$ and $\tau = 0.3$. The maximum energy growth was found at $\beta = 400\pi$. Both time horizons show a significant energy transient growth phenomena, but, but for $\tau = 0.1$ the optimal perturbation is a thin shear layer, localised nearby the separation bubble, while a row of alternating vortices, typical of a Kelvin–Helmholtz instability was found at $\tau = 0.3$.

Conflict of interest statement

The authors declare that there is no conflict of interests regarding the publication of this article.

Acknowledgements

References

[1] N. Abdessemed, S.J. Sherwin, V. Theofilis, Linear instability analysis of low-pressure turbine flows, J. Fluid Mech. 628 (2009) 57–83.
[2] D. Barkley, Linear analysis of the cylinder wake mean flow, Europhys. Lett. 75 (5) (2006) 750–756s.
[3] D. Barkley, H.M. Blackburn, S.J. Sherwin, Direct optimal growth analysis for timesteppers, Int. J. Numer. Methods Fluids 57 (2008) 1435–1458.
[4] H.M. Blackburn, D. Barkley, S.J. Sherwin, Convective instabilities and transient growth in a flow over a backward-facing step, J. Fluid Mech. 603 (2008) 271–304.
[5] B. Cantwell, D. Coles, An experimental study of entrainment and transport in the turbulent near wake of a circular cylinder, J. Fluid Mech. 136 (1983) 321–374.
[6] L. Hilgenfeld, M. Pfitzner, Unsteady boundary development due to wake passing effects on a highly loaded linear compressor cascade, J. Turbomach. 493 (2004) 493–500.
[7] J.D. Hughes, G.J. Walker, Natural transition phenomena on an axial flow compressor blade, J. Turbomach. 123 (2001) 392–401.
[8] M. Israeli, S.A. Orszag, Approximation of radiation boundary conditions, J. Comput. Phys. 41 (1981) 115–135.
[9] L.E. Jones, R.D. Sandberg, N.D. Sandham, Direct numerical simulations of forced and unforced separation bubbles on a airfoil at incidence, J. Fluid Mech. 602 (2008) 175–207.
[10] G.E. Karniadakis, M. Israeli, S.A. Orszag, High-order splitting methods for incompressible Navier–Stokes equations, J. Comput. Phys. 97 (1991) 414.
[11] G.E. Karniadakis, S.J. Sherwin, Spectral/hp Element Methods for Computational Fluid Dynamics, 2nd edn., Oxford University Press, 2005.
[12] H. Schreiber, W. Steinert, T. Sonoda, T. Arima, Advanced high turning compressor airfoils for low Reynolds number condition. Part II: experimental and numerical analysis, J. Turbomach. 126 (4) (2004) 482–492.
[13] T. Sonoda, Y. Yamaguchi, T. Arima, M. Olhoder, B. Sendhoff, H.A. Schreiber, Advanced high turning compressor airfoils for low Reynolds number. Part I: design and optimization, J. Turbomach. 126 (3) (2004) 350–359.
[14] V. Theofilis, Global linear instability, Annu. Rev. Fluid Mech. 43 (2011) 319–352.
[15] L.S. Tuckerman, D. Barkley, Bifurcation analysis for timesteppers, in: Numerical Methods for Bifurcation Problems and Large-Scale Dynamical Systems, 2000.
[16] J.G. Wissink, W. Rodi, Direct numerical simulation of flow and heat transfer in a turbine cascade with incoming wakes, J. Fluid Mech. 596 (2006) 209–247.
[17] X. Wu, P.A. Durbin, Evidence of longitudinal vortices evolved from distorted wakes in a turbine passage, J. Fluid Mech. 446 (2001) 199–228.
[18] T.A. Zaki, P.A. Durbin, Mode interaction and the bypass route to transition, J. Fluid Mech. 531 (2005) 85–111.
[19] T.A. Zaki, J.C. Wissink, P.A. Durbin, W. Rodi, Direct computations of boundary layers distorted by migrating wakes in a linear compressor cascade, Flow Turbul. Combust. 83 (2009) 307–322.
[20] T.A. Zaki, J.G. Wissink, W. Rodi, P. Durbin, Direct numerical simulations of transition in a compressor cascade: the influence of free-stream turbulence, J. Fluid Mech. 665 (2010) 57–98.